【発表に関する最新情報】

English

厚生労働科学研究費補助金 医療機器開発推進研究事業

深部機能画像診断のための光音響画像化技術の有用性検証 研究成果公表サイト

ホーム 研究について 研究体制 研究紹介 研究論文一覧 発表に関する最新情報 お問合せ

発表に関する最新情報

2014年10月15日～18日
第87回日本生化学会大会（国立京都国際会館）

2013年11月8日
第27回日本泌尿器内視鏡学会総会
（特別企画）未来の名匠を発掘する4 医工連携への取り組み
「根治的前立腺全摘術における的確な神経温存のための光音響画像化技術の有用性」（堀口明男）

2013年10月17日
第5回 BioOpto Japan
カンファレンス テーマ2「再生医療と光技術」
「再生医療を評価する光計測技術」（石原 美弥）

平成25年10月3日
平成25年度 第2回 光超音波画像研究会
「光音響イメージングにおける周波数成分に関する検討」（石原 美弥）

2013年9月5日
第8 回In vivo イメージングフォーラム2013
「光と超音波の特長を併せ持つ光音響断層イメージングの基礎から最先端応用まで」（石原 美弥）

2013年9月
光アライアンス24(9)
「光音響法を用いた生体計測技術」（石原美弥）

2013年9月
日本レーザー医学会誌34(1)
「光音響（光超音波）画像の最前線②」の特集によせて」（石原 美弥）

2013年9月
日本レーザー医学会誌34(1)
「【総説】光音響イメージングの最近の進展」（石原 美弥）

2013年9月
日本レーザー医学会誌34(1)
「前立腺癌に対する光音響イメージングを用いた局在診断の可能性」（堀口 明男, 淺野 友彦）

2013年8月2日
平成25年度 第1回 光超音波画像研究会
【特別講演】「光超音波(光音響)画像診断におけるレーザー安全に関する基礎検討」（石原美弥）

2013年8月2日
平成25年度 第1回 光超音波画像研究会
「光音響イメージング装置―光音響画像と超音波画像の融合―」（辻田和宏, 入澤 覚, 広田和弘, 平沢 壮, 藤田真敬, 石原美弥）

2013年8月
レーザー研究41(8)
「癌診断のための光音響イメージング技術」（樽引俊宏, 石原美弥）

2013年1月
日本レーザー医学会誌33(4)
「「光音響(光超音波)画像の最前線」の特集によせて」（石原美弥）

2013年1月
日本レーザー医学会誌33(4)
「細胞観察のための光音響イメージング顕微鏡」（樽引俊宏, 石原美弥）

▲ ページ上部へ

【お問合せ】

B. アクセス数レポート

表１　月別訪問数

月	訪問数
2013 年　10 月	77
2013 年　11 月	72
2013 年　12 月	59
2014 年　1 月	97
2014 年　2 月	48

表２　キーワード別の訪問数と訪問別ページビュー

キーワード	訪問数	訪問別ページビュー
(not provided) ※	142	2.83
大谷直樹教授	22	1.55
藤田真敬	4	3.00
光超音波 イメージング	3	7.67
厚生労働科学研究費補助金	3	1.00
厚労 光音響	3	4.33
富士フイルム(株) r&d 統括本部 メディカルシステム開発センター 辻田	3	7.33
石原美弥	2	8.00
bioopto japan 石原美弥	1	2.00
photoacoustic imaging 論文	1	1.00

※　(not provided)とはキーワードが不明という表示。
google で検索した場合，google が訪問者の入力したキーワードを暗号化するために不明となる。

Ⅳ.　研究成果の刊行（平成 25 年度）に関する一覧

論文

発表者氏名	論文タイトル名	発表誌名	巻号	ページ	出版年
Otani N, Ishihara M, Nakai K, Fujita M, Wada K, Mori K	Uncooled infrared camera for the noninvasive visualization of the vascular flow in an anastomotic vessel during neurological surgery: Technical Note	Neurologia medico-chirurgica			[Epub ahead of print]
Ishihara M, Hirasawa T, Okawa S, Sato R, Urano Y, Teranishi T	The effect of surface charge of plasmonic gold nanoparticles on photoacoustic signal	Proceedings of SPIE	8943	89434D-1-89434D-6	2014年3月
Okawa S, Hirasawa T, Kushibiki T, Ishihara M	Reconstruction of the optical absorption coefficient from photoacoustic signals measured by scanning coaxial probe with regularization methods	Proceedings of SPIE	8943	89433W-1-89433W-8	2014年3月
Hirasawa T, Okawa S, Fujita M, Kushibiki T, Ishihara M	Quantification of optical attenuation coefficient based on continuous wavelet transform of photoacoustic signals measured by a focused broadband acoustic sensor	Proceedings of SPIE	8943	89435Z-1-189435Z-10	2014年3月
Hirasawa T, Fujita M, Okawa S, Kushibiki T, Ishihara M	Quantification of effective attenuation coefficients using continuous wavelet transform of photoacoustic signals	Applied Optics	52(35)	8562-8571	2013年12月
石原美弥	光音響信号の周波数成分が画像性能に与える影響	電気学会研究会資料 光・量子デバイス研究会資料	OQD-13-047	27-29	2013年11月
Okawa S, Hirasawa T, Kushibiki T, Ishihara M	Numerical evaluation of linearized image reconstruction based on finite element method for biomedical photoacoustic imaging	Optical Review	20(5)	442-451	2013年10月
Ishihara M, Okawa S, Sato R, Hirasawa T, Teranishi T	Photoacoustic signal enhancement by localized surface plasmon of gold nanoparticles	Proceedings of the International Conference Nanomaterials:	2(4)	04NABM12-1-04NABM12-3	2013年8月

発表者氏名	論文タイトル名	発表誌名	巻号	ページ	出版年
		Applications and Properties			
堀口明男, 淺野友彦	前立腺癌に対する光音響イメージングを用いた局在診断の可能性	日本レーザー医学会誌	34(1)	19-23	2013年6月
辻田和宏	光音響イメージングの医療応用に向けて –光音響画像と超音波画像の融合–	レーザー医学会誌	33(4)	380-385	2013年1月
櫛引俊宏, 石原美弥	細胞観察のための光音響イメージング顕微鏡	レーザー医学会誌	33(4)	392-398	2013年1月

学会発表

発表者氏名	発表タイトル名	学会名	抄録誌名	ページ	発表年
Ishihara M, Hirasawa T, Okawa S, Sato R, Urano Y, Teranishi T	The effect of surface charge of plasmonic gold nanoparticles on photoacoustic signal	SPIE Photonics West Biomedical Optics, BiOS 2014	SPIE Photonics West BiOS 2014 Technical Summaries	305	2014年2月
Okawa S, Hirasawa T, Kushibiki T, Ishihara M	Reconstruction of the optical absorption coefficient from photoacoustic signals measured by scanning coaxial probe with regularization methods	SPIE Photonics West Biomedical Optics, BiOS 2014	SPIE Photonics West BiOS 2014 Technical Summaries	294	2014年2月
Hirasawa T, Okawa S, Fujita M, Kushibiki T, Ishihara M	Quantification of optical attenuation coefficient based on continuous wavelet transform of photoacoustic signals measured by a focused broadband acoustic sensor	SPIE Photonics West Biomedical Optics, BiOS 2014	SPIE Photonics West BiOS 2014 Technical Summaries	326	2014年2月

発表者氏名	発表タイトル名	学会名	抄録誌名	ページ	発表年
大川晋平, 平沢壮, 櫛引俊宏, 石原美弥	光音響技術による分子イメージングと光伝播を考慮した定量的画像再構成	第36回日本分子生物学会年会	第36回日本分子生物学会年会要旨集	3AW2-7-3 AW2-7	2013年12月
石原美弥	光音響信号の周波数成分が画像性能に与える影響	電気学会光・量子デバイス研究会	電気学会研究会資料 光・量子デバイス研究会 OQD-13-047	27-29	2013年11月
堀口明男, 伊藤敬一, 浅野友彦, 川口真, 辻田和宏, 石原美弥	根治的前立腺全摘術における的確な神経温存のための光音響画像化技術の有用性	第27回日本泌尿器内視鏡学会総会	Japanese Journal of Endourology 26(3)	189	2013年11月
Ishihara M, Okawa S, Sato R, Hirasawa T, Teranishi T	Photoacoustic signal enhancement by localized surface plasmon of gold nanoparticles	Nanomaterials:Application & Properties '2013	Nanomaterials:Application & Properties '2013 Program	43	2013年9月
石原美弥	光と超音波の特長を併せ持つ光音響断層イメージングの基礎から最先端応用まで	第8回In vivoイメージングフォーラム2013	第8回In vivoイメージングフォーラム2013	16-17	2013年9月
石原美弥	【特別講演】光超音波(光音響)画像診断におけるレーザー安全に関する基礎検討	第1回光超音波画像研究会	第1回光超音波画像研究会プログラム　抄録集	1	2013年8月
辻田和宏, 入澤覚, 広田和弘, 平沢壮, 藤田真敬, 石原美弥	光音響イメージング装置—光音響画像と超音波画像の融合—	第1回光超音波画像研究会	第1回光超音波画像研究会プログラム　抄録集	6	2013年8月
Ishihara M, Hirasawa T, Sato R, Okawa S, Teranishi T	Characterization of photoacoustic signal of plasmonic gold nanoparticles	CLEO-PR & OECC/PS 2013	CLEO-PR & OECC/PS 2013 Conference Program & Abstracts	196	2013年7月
Okawa S, Hirasawa T, Kushibiki T, Ishihara M	Comparison of regularization methods for photoacoustic image reconstruction	Conference on Laser Surgery and Medicine 2013	Proceedings of Conference on Laser Surgery and Medicine 2013	34-35	2013年4月

その他

発表者氏名	タイトル名	発表誌名	巻号	ページ	出版年
石原美弥	光音響法を用いた生体計測技術	光アライアンス	24(9)	12-14	2013年9月
石原美弥	「光音響(光超音波)画像の最前線②」の特集によせて	日本レーザー医学会誌	34(1)	9	2013年6月
石原美弥	光音響イメージングの最近の進展	日本レーザー医学会誌	34(1)	10-13	2013年6月
石井克典, 橋村圭亮, 北哲也, 粟津邦夫, 近江雅人, 平沢壮, 石原美弥	国際会議報告 Photonics West BiOS 2013	日本レーザー医学会誌	34(1)	50-54	2013年6月
石原美弥	「光音響(光超音波) 画像の最前線」の特集によせて	日本レーザー医学会誌	33(4)	366	2013年1月

V. 研究成果の刊行・別刷

Reconstruction of the optical absorption coefficient from photoacoustic signals measured by scanning coaxial probe with regularization methods

Shinpei Okawa, Takeshi Hirasawa, Toshihiro Kushibiki and Miya Ishihara

Department of Medical Engineering, National Defense Medical College, 3-2 Namiki, Tokorozawa, Saitama, 359-8513, Japan

ABSTRACT

Reconstruction of the absorption coefficient from photoacoustic signals is discussed. The photoacoustic (PA) signals were acquired by using a ring-shaped P(VDF-TrFE) acoustic sensor coaxially arranged with an optical fiber. The acoustic sensor scanned the measured object. The linearized image reconstruction method previously presented by the authors was modified for the measurement with the coaxial probe. The distribution of the absorption coefficient was reconstructed by solving the inverse problem based on the PA wave equation and the photon diffusion equation. The linearized forward model was formulated by solving the partial differential equations with finite element method. To eliminate the effect of the unknown background on the PA signal, the differences between the PA signals measured at different positions were used for the image reconstruction. The image reconstruction method was validated by numerical and phantom experiments. Moreover, the reconstructed images with the Tikhonov and l_p sparsity regularization methods were compared from the standpoints of spatial resolution, robustness to noise and quantification of the absorption coefficient.

Keywords: photoacoustic tomography, P(VDF-TrFE), absorption coefficient, regularization, inverse problem

1. INTRODUCTION

Photoacoustic (PA) imaging[1,2] enables us to diagnose the tissues deep inside the biological medium quantitatively. In PA imaging, nano-second pulse laser illuminates biological tissues, and then the energy of the light absorbed by photon absorber such as hemoglobin is converted into heat. As a result, the thermal expansion of the photon absorber generates elastic wave called PA pressure. The PA pressure depends on the optical absorption coefficients of the photon absorber. Therefore, by calculating the absorption coefficient from the PA signals, quantitative information inside the biological tissue which can be useful for medical diagnoses is obtained.

Although, PA technique images shallow regions because of the limited penetration depth of the excitation light, PA imaging takes advantage of ultrasound imaging and has high spatial resolution from 10 μm to 1 mm. PA signal is not affected by the inhomogeneity of the biological media so much, compared with the light. And also by exploiting the principle of the biomedical measurement using light, PA imaging obtains spectroscopic information which can not be available for ultrasound imaging.

PA image is reconstructed by various techniques. Delay-and-sum backprojection and circular backprojection originally developed for ultrasound imaging can readily be implemented. Frequency-domain reconstruction and universal backprojection which are analytically derived from wave equation were presented by Xu et al.[2] Those analytical reconstruction methods function well in the acoustically homogeneous medium. $k-$space method efficiently calculates the forward solution PA propagation in frequency domain. By using $k-$space pseudospectral methods, Treeby et al reconstructed high-quality image of the vasculature by time-reversal method and compensating the acoustic absorption in acoustically heterogeneous medium.[3]

By taking account of the excitation light propagation, the optical properties and concentrations of the chromophores in optically inhomogeneous medium can be estimated.[4,5] Laufer et al achieved model-based inversion scheme reconstructing the chromophore concentration. This method minimizes the error between the measured and predicted images by using the forward model with photon diffusion equation (PDE) for light propagation and

Shinpei Okawa: E-mail: okawa@ndmc.ac.jp, Telephone: +81 4 2995 1596

Photons Plus Ultrasound: Imaging and Sensing 2014, edited by Alexander A. Oraevsky, Lihong V. Wang,
Proc. of SPIE Vol. 8943, 89433W · © 2014 SPIE · CCC code: 1605-7422/14/$18 · doi: 10.1117/12.2041249

$k-$space method for acoustic wave propagation.[6] Yuan et al reconstructs the optical absorption coefficient using PDE and finite element method (FEM) based PA image reconstruction algorithm.[7] Okawa et al. constructed a linearized reconstruction method based on FEM and numerically investigated the performance.[8]

In this paper, we attempted to reconstruct the distribution of the absorption coefficient from the PA signals acquired by the probe which has coaxially arranged optical fiber to illuminate the measurement object and piezoelectric film to detect PA pressure. The probe scanned the surface of the measured object and measured the PA signals at multiple positions. Then the measured PA signals were used to reconstruct the absorption coefficient. The reconstruction was carried out by solving the inverse problem. The PA forward model was constructed by PA wave equation, and the propagation of the light is taken into account by using PDE. Both equations were solved by FEM. Then the relation between the detected PA signal and the optical properties in the medium was formulated as a linear equation. The image is reconstructed by minimizing the error between the detected and calculated PA signals. In this study, the linearized image reconstruction method previously presented by the authors[9] was modified for the measurement with the coaxial probe. And the differences between the PA signals measured at different positions were used for the reconstruction to eliminate the effect of the unknown background on the PA signals. The numerical and phantom experiments validated the image reconstruction method.

The reconstructed image includes artifacts due to measurement noise and imperfect FEM forward modeling. The ill-posed nature of the inverse problem aggravates the artifacts. A simple forward model, however, is preferable in the sense of the computational cost for practical use. The regularization is one of the useful approaches to reduce the artifacts. The Tikhonov and l_1 sparsity regularizations[9–11] were used in the reconstruction. The regularization methods were compared numerically and experimentally in this study.

2. FORWARD MODELING

2.1 PA pressure propagation

As the nano-second pulse laser illuminates the measured biological medium, the light propagates in the biological medium and is absorbed by the photon absorber such as hemoglobin. And the absorbed light energy is converted into the heat, which generates the PA pressure. When the conditions of the thermal and stress confinements are met, the PA pressure is efficiently generated. The propagation of the PA pressure in an acoustically homogeneous medium is described by the following wave equation,[2]

$$\left\{-\nabla^2 + \frac{1}{v^2}\frac{\partial^2}{\partial t^2}\right\} p(r,t) = \hat{\Gamma}\frac{\partial}{\partial t}H, \tag{1}$$

where v is the speed of the PA pressure p, $\hat{\Gamma}$, Grüneisen parameter associated with the PA efficiency, H, absorbed energy density, and r, the position. The PA source term is the energy of the light absorbed by tissues, which can be calculated by solving following photon diffusion equation. FEM is employed to solve this forward problem in this study.

2.2 Light propagation

The source of the PA signal depends on the distributions of the fluence rate of the light and the absorption coefficient. The absorbed energy density is given by $H = \mu_a\Phi$ with the absorption coefficient μ_a and the fluence rate Φ, which are calculated with PDE.[5] The PA sources are not only diagnostically interesting tissues such as tumor with highly-concentrated blood but also the surrounding normal tissues termed "background" in this study.

The light is scattered and absorbed by biological tissues. The propagation of the excitation light is described by the radiative transfer equation (RTE).[5] In this paper, we use following time-independent PDE which is the approximation of RTE,

$$\{-\nabla \cdot D(r)\nabla + \mu_a(r)\}\,\Phi(r) = q_0(r), \tag{2}$$

where D is the diffusion coefficient, μ_a, the absorption coefficient, Φ, the fluence rate of light, q_0, the light source. PDE is hold when the medium is thick enough and the time after the pulse light incidence is longer. The

boundary condition is given as $-n \cdot D\nabla\Phi = 1/(2A)\Phi$ where n is the vector normal to the surface of the medium, and A is the parameter depending on the internal reflection ratio. PDE can be solved by using FEM.

2.3 Forward formulation for reconstruction from measurements with coaxial probe

The PA signal is measured by the probe which has the coaxially arranged optical fiber as the light source and piezoelectric film as the detector. That means that the illuminating and detecting positions are identical. Let us assume that the probe illuminates the light at the upper surface of the measured object and that the detector has high directivity and is sensitive to the PA pressure generated by the PA sources located directly below the coaxial probe. Equation (1) indicates that the detected PA signal is linearly related with the PA source term. Therefore, following linear equation relates the PA signals measured at k-th position to the PA sources just below the probe,

$$\boldsymbol{m}_k = L_k \boldsymbol{H}_k, \tag{3}$$

where $\boldsymbol{m}_k$ is a T-vector of the set of PA signals with T time samples measured by the coaxial probe at k-th position, and $\boldsymbol{H}_k$ is an M-vector of the PA source below the probe spatially discretized into M pixels. L_k is a $T \times M$-matrix representing the contributions of the discretized sources to the measured signals. L_k is obtained by calculating PA signals generated by each of the sources with a unit strength.

$\boldsymbol{H}_k$ is described as a first-order Talor expansion about the background absorption coefficient $\bar{\mu}_a$. Then, Eq.(3) is rewritten to relate $\boldsymbol{m}_k$ and μ_a as,

$$\boldsymbol{m}_k = L_k \left(\bar{\boldsymbol{H}}_k(\bar{\mu}_a) + J_k \Delta\mu_a \right), \tag{4}$$

where $\bar{\boldsymbol{H}}_k$ is the PA source generated by the background absorption and $\Delta\mu_a$ is an N-vector of the distribution of the perturbation of μ_a in the whole of medium discretized into N pixels. J_k is the matrix consists of the differential coefficients of $\boldsymbol{H}_k$ at $\bar{\mu}_a$ and is calculated by perturbation method using FEM with Eq.(2).

In this study, we attempt to reconstruct $\Delta\mu_a$. The large change in μ_a can indicate the diseased tissue such as cancer with angiogenesis. The difference between PA signals measured at different two positions are used for the reconstruction to eliminate the effect of the unknown $\bar{\mu}_a$ on PA signals. By assuming that the medium is so large that the baundary effect on the measurement is negligible, $L_k \bar{\boldsymbol{H}}_k \simeq L_l \bar{\boldsymbol{H}}_l$, $(k \neq l)$. Then we obtain,

$$\begin{aligned} \Delta\boldsymbol{m}_{k,l} &= \boldsymbol{m}_k - \boldsymbol{m}_l \\ &= (L_k J_k - L_l J_l)\, \Delta\mu_a \\ &= G_{k,l} \Delta\mu_a. \end{aligned} \tag{5}$$

The reconstruction of $\Delta\mu_a$ is conducted with the following forward equation,

$$\Delta\boldsymbol{m} = G\Delta\mu_a, \tag{6}$$

where $\Delta\boldsymbol{m}$ is the vector consists of $\Delta\boldsymbol{m}_{k,l}$, and G is the matrix consists of $G_{k,l}$.

In this study, the detected PA signals and the matrix G were down-sampled to reduce the calculation cost for efficient reconstruction. Considering the pixel size, it is not necessary to use all temporal samples of the PA signal. We sampled the datum which had the maximum absolute value of the PA signal in every interval of 0.133 μs (= 2 mm / 1.5 mm $\cdot$ μs^{-1}) as the signal for the reconstruction under the assumption that the signal-to-noise ratio was sufficiently high.

3. IMAGE RECONSTRUCTION

3.1 Reconstruction with Tikhonov regularization

The reconstruction of $\Delta\mu_a$ is carried out by solving the optimization problem with the Tikhonov regularization,[10]

$$\min_{\Delta\mu_a} \left\| \Delta\boldsymbol{m} - G\Delta\mu_a \right\|^2 + \lambda \cdot \left\| \Delta\mu_a \right\|^2, \tag{7}$$

where $\Delta\boldsymbol{m}$ is composed of the PA signals measured at multiple positions and λ is a regularization parameter to adjust the effect of the regularization term on the reconstruction. Then the reconstructed $\widehat{\Delta\mu}_a$ is obtained as,

$$\widehat{\Delta\mu}_a = \left(G^T G + \lambda \cdot I \right)^{-1} G^T \Delta\boldsymbol{m}. \tag{8}$$

3.2 Reconstruction with l_p sparsity regularization

A sparse solution is obtained by using the l_p sparsity regularization[11] which minimizes the p-norm of the solution with the residual error. The spatial resolution of the reconstructed image with l_p sparsity regularization is higher than that with the Tikhonov regularization.[9,11] The image reconstruction with the l_p sparsity regularization in this study is described as follows,

$$\min_{\Delta\mu_a} \|\Delta \boldsymbol{m} - G\Delta\mu_a\|^2 + \lambda \cdot f(\Delta\mu_a), \tag{9}$$

where f is a regularization term and λ is a regularization parameter.

l_p sparsity regularization employs f of the p-norm of $\Delta\mu_a$,

$$f = \sum_{i=1}^{M} |\Delta\mu_{a_i}|^p, \tag{10}$$

where $0 < p \leq 2$. When $p \leq 2$, it is problematic to calculate the gradient of f for non-linear gradient based optimization. So, $\Delta\mu_{a_i}$ is expressed by a parameter z_i,[11]

$$\Delta\mu_{a_i} = |z_i|^{2/p} \cdot \mathrm{sgn}(z_i). \tag{11}$$

Then the optimization problem Eq.(6) is rewritten as,

$$\min_{\boldsymbol{z}} \|\Delta \boldsymbol{m} - G\Delta\mu_a(\boldsymbol{z})\|^2 + \lambda \cdot \sum_{i=1}^{M} |z_i|^2. \tag{12}$$

By solving the optimization problem in Eq.(9), $\widehat{\Delta\mu_a}$ is reconstructed. It is expected that the l_p sparsity regularization with $p < 2$ provides a sparse solution, and the spatial resolution of the reconstructed image is improved. $p = 1$ was used in this study.

4. CONDITIONS OF NUMERICAL SIMULATION AND PHANTOM EXPERIMENT

4.1 Numerical simulation

In the numerical simulation, the spatial resolution and the quantification ability of the reconstructions with the Tikhonov regularization and the l_p sparsity regularization were compared.

Figure 1(a) shows 2D geometry used in the numerical simulations. The medium was a square region with 50 mm side. The illuminating and detecting positions were identical. The PA signals were measured at 11 positions of $x = -10,\ -8,\ \cdots,\ 10$ mm on $y = 0$ mm. The light source with a wavelength in NIR range was assumed, and the optical properties of the background medium are uniformly distributed with $\bar{\mu}_s' = 0.8$ mm^{-1} and $\bar{\mu}_a = 0.01$ mm^{-1}. The target, which had μ_a larger than that of the background, was placed in the medium. The position of the target was y =20 or 18 mm on $x = 0$ mm. The target was a circle with 1 mm diameter. The reconstructions were conducted when the target had μ_a of 0.1, 0.2, 0.5 or 1.0 mm^{-1}. We attempted to reconstruct $\Delta\mu_a$ by the Tikhonov and the l_p sparsity regularizations.

FEM was used with 10,201 nodes and 20,000 triangular elements to simulate PA signals. The FEM nodes were distributed uniformly with an equal spacing of 0.5 mm. The speed of the PA pressure in the medium of 1.5 mm/μs was used for the FEM calculation, and Grüneissen parameter was set as unity. The time-dependent terms in eq.(2) was calculated by differential approximation with time step of $\Delta t = 0.1$ μs. Equation (2) discretized by FEM was solved with implicit scheme. We assumed that measurement period was 50 μs.

We carried out the image reconstruction on pixel basis. The medium was discretized into 625 pixels. Every pixel with 2 mm side contained 25 FEM nodes. The PA signals generated by the sources at FEM nodes in a single pixel was averaged and was used as the contribution (a single column of the matrix L_k) of a single-pixel PA source to the measurement data. The component of J_k was also the average over the nodes in a single pixel. The regularization parameter was selected empirically.

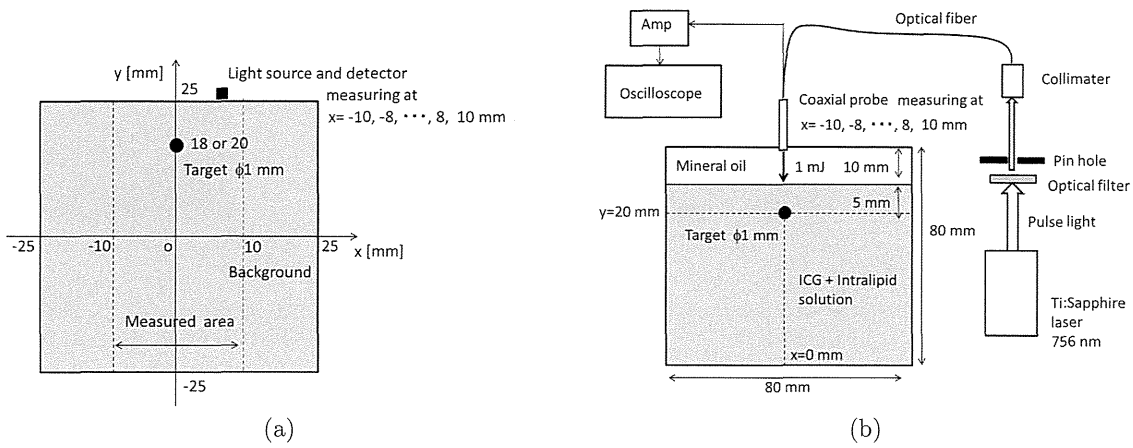

Figure 1. (a) 2D geometries for numerical simulation and (b) Schematic chart of the phantom experiment.

4.2 Phantom experiment

The improvement in localization of the target reconstructed by the l_p sparsity regularization was demonstrated by comparing the Tikhonov regularization in the phantom experiment.

Figure 1(b) illustrates the schematic chart of the phantom experiment. A tunable Ti:sapphire laser (LT-2211, Lotis Tii, Minsk, Belarus) pumped by the second harmonic of a Q-switched Nd:YAG laser (LS-2134, Lotis Tii, Minsk, Belarus) was used to produce excitation light pulses with a width of about 10 ns and a repetition frequency of 15 Hz at 756 nm. The light pulse was coupled into a multi-mode optical fiber (M41L02, Thorlabs, Newton, NJ) with a core diameter of 0.6 mm. The optical fiber was introduced into a cylindrical probe which had a ring shaped piezoelectric film P(VDF-TrFE) (KF piezo-film, Kureha Corp., Tokyo, Japan) on the detecting surface. The film had a thickness of 20 μm. The edge of the optical fiber, from which the light pulse of 1 mJ was emitted, was located at the center of the film, and the light source and the detector were coaxially arranged. The detected PA signal was amplified by the noise field-effect transistor amplifier (SA-220FS, NF Electronic Instruments, Yokohama, Japan), and recorded by a digital oscilloscope (DSO7104A, Agilent Technologies, Santa Clara, CA). The PA signals were averaged over 100 light pulses online. The sampling rate was 20 MHz. $\Delta\mu_a$ was processed with offline lowpass filter with a cutoff frequency of 4.6 MHz. The image reconstructions were conducted with the same manner in the numerical simulation.

The measured object was a liquid phantom made of intralipid and indocyanine green (ICG) diluted with water. The optical properties of the phantom was adjusted to $\mu_s' = 0.8$ mm^{-1} and $\mu_a = 0.01$ mm^{-1}. There existed a target in the phantom. The target was a polybutadien tube containing diluted intralipid and ICG. The optical properties of the target were $\mu_s' = 0.8$ mm^{-1} and $\mu_a = 0.62$ mm^{-1}.[12]

5. RESULTS AND DISCUSSIONS

5.1 Numerical simulation

The reconstructed images when the true target was at $(x,\ y) = (0$ mm, 18 mm$)$ are shown in Fig. 2(a) and (b). The Tikhonov regularization reconstructed maximum of $\widehat{\Delta\mu_a}$ at the true position of the target. However, the distribution of $\Delta\mu_a$ broadened and the target was reconstructed at the correct position and the pixels at neighboring to the true position. The Tikhonov regularization provides the smooth solution. Therefore, it is difficult to obtain sparse high resolved image with the Tikhonov regularization. The maximum of $\widehat{\Delta\mu_a}$ was about $1.2\times\ 10^{-3}$ mm^{-1}.

On the other hand, by the l_p sparsity regularization, the target was reconstructed in a single pixel at the true position of the target as shown in Fig. 2(b). The maximum of $\widehat{\Delta\mu_a}$, about 0.04 mm^{-1}, was 4 times larger than that reconstructed by the Tikhonov regularization. By localizing the PA source in a small area, the strength of the PA source became larger.

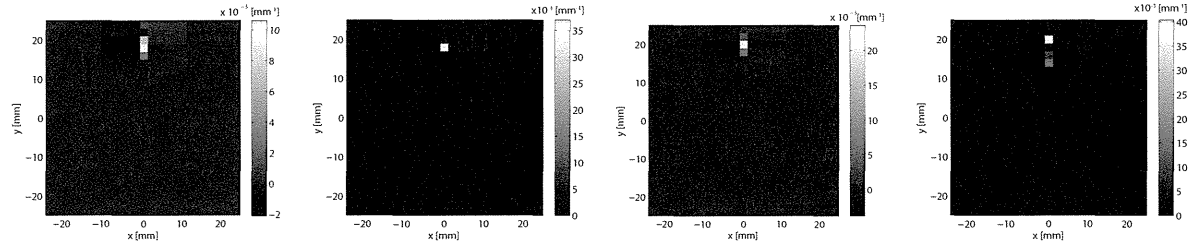

Figure 2. The reconstructed images with (a) theTikhonov and (b) the l_p sparsity regularizations when the true target was at $(x,\ y) = (0\text{ mm},\ 18\text{ mm})$ and with (c) the Tikhonov and (d) the l_p sparsity regularizations when the true target was at $(x,\ y) = (0\text{ mm},\ 20\text{ mm})$ in the numerical simulation.

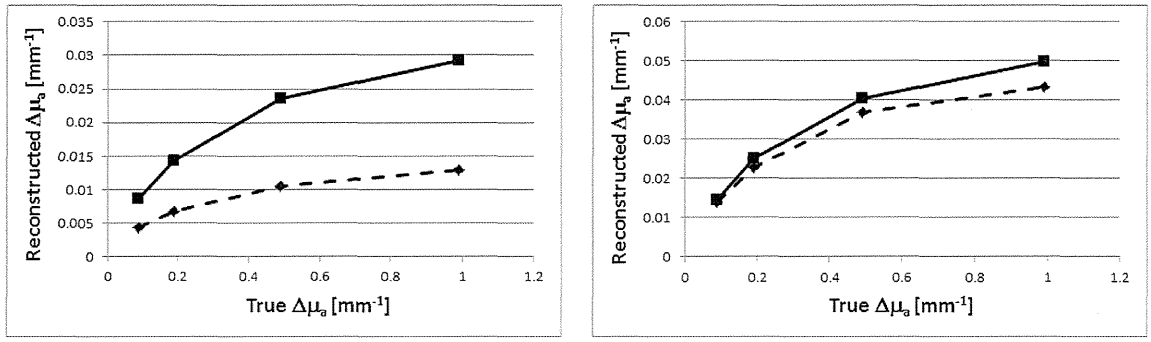

Figure 3. The reconstructed $\Delta\mu_a$ with (a) the Tikhonov and (b) the l_p sparsity regularizations as a function of true $\Delta\mu_a$ when the true target was at $(x,\ y) = (0\text{ mm},\ 18\text{ mm})$ (dashed line) or $(x,\ y) = (0\text{ mm},\ 20\text{ mm})$ (solid line).

The target reconstructed at the correct position by the Tikhonov regularization was well localized when the true target was at $(x,\ y) = (0\text{ mm},\ 20\text{ mm})$. The l_p sparsity regularization increased the value of $\widehat{\Delta\mu_a}$. The reconstructed value of $\widehat{\Delta\mu_a}$ was much smaller than true one, because the pixel size was larger than the target size and the reconstructed $\widehat{\Delta\mu_a}$ was deconcentrated. The regularizations were also causes of the underestimation of the $\widehat{\Delta\mu_a}$. The smaller the reconstructed values, the smaller the regularization terms in Eqs.(7) and (12).

Figure 3(a) shows the maximum of $\widehat{\Delta\mu_a}$ with the Tikhonov regularization as a function of true $\Delta\mu_a$. Although the true $\Delta\mu_a$ was same, $\widehat{\Delta\mu_a}$ in $y = 18$ mm was smaller than that in $y = 20$ mm when the reconstruction was carried out with the Tikhonov regularization. That was because the reconstructed target at $y = 18$ mm broadened more than that at $y = 20$ and the strength of the PA source was deconcentrated. Although decreasing Φ owing to the scattering and the absorption by the medium was taken into account for the reconstruction by employing PDE, $\widehat{\Delta\mu_a}$ depended on the depth from the surface. It is difficult to quantify the absorption coefficient because of the nature of the inverse problem.

By localizing $\widehat{\Delta\mu_a}$ by using the l_p sparsity regularization and by alleviating the deconcentration, the difference between the reconstructed targets at $y = 18$ mm and $y = 20$ mm became smaller as shown in Fig. 3(b). The quantitative ability of the image reconstruction was improved by the l_p sparsity regularization. The relative error between $\widehat{\Delta\mu_a}$ at $y = 18$ and $y = 20$ mm were decreased from about 32 % to 1%. The reconstructed $\widehat{\Delta\mu_a}$ did not linearly depend on the true values. The linearization in the forward modeling implied that $\Delta\mu_a$ was small. Therefore, the large changes in μ_a were not reconstructed correctly by the linearized reconstruction method.

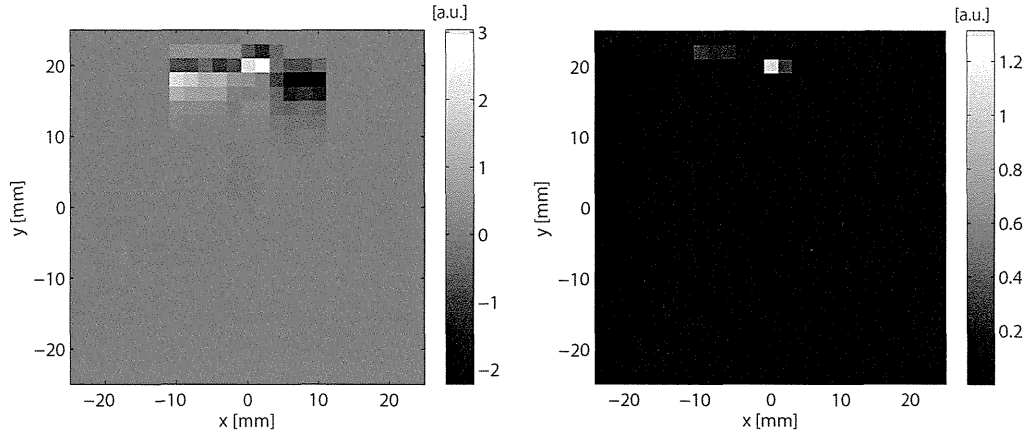

Figure 4. The reconstructed images with (a) the Tikhonov and (b) the l_p sparsity regularizations when the true target was at $(x,\ y) = (0\text{ mm},\ 20\text{ mm})$.

5.2 Phantom experiment

Figure 4 shows the reconstructed images in the phantom experiment. The target at $(x,\ y) = (0\text{ mm},\ 20\text{ mm})$ is found in the image reconstructed by the Tikhonov regularization in Fig. 4(a). The reconstruceted target was broadened and astride the two pixels. One of the possible reasons was the real detector did not have the ideal high directivity and detected the PA signals from the PA sources which was not directly below the detector. Noise caused the artifacts in the reconstructed image.

On the other hand, the target was clearly reconstructed by the l_p sparsity regularization. Although some small artifacts can be seen in the reconstructed image in Fig. 4(b), the target reconstructed by the l_p sparsity regularization was localized more than that by the Tikhonov regularization. $\widehat{\Delta\mu_a}$ with the l_p sparsity regularization did not become larger than that with the Tikhonov regularization in the phantom experiment. Measurement noises and the selection of the regularization parameter might make the differences between the phantom experiment and the numerical simulation.

The improvement in localization of the target reconstructed by the l_p sparsity regularization was successfully demonstrated by the phantom experiment. To investigate the effects of the l_p sparsity regularization on the PA image reconstruction experimentally, more precise experiments may be needed.

6. CONCLUSION

The reconstruction of the optical coefficient from the photoacoustic signals measured by a coaxial probe was tried in this study. The probe had a ring shaped P(VDF-TrFE) film to detect the acoustic signal and the optical fiber to illuminate the measured object coaxially. By eliminating the PA signals generated by the background, the changes in the absorption coefficient were reconstructed by solving the linearized inverse problem in the numerical simulation and phantom experiment. The Tikhonov and l_p sparsity regularizations were used and compared. The l_p sparsity regularization improved the localization of the reconstructed target in the numerical simulation and the phantom experiment. It was shown in the numerical simulation that the quantification ability of the reconstructed target was also improved.

ACKNOWLEDGEMENTS

This work was supported in part by JST Collaborative Research Based on Industrial Demand (In vivo Molecular Imaging: Towards Biophotonics in Medicine) and JSPS KAKENHI Grant Number 24760314. Finally, we would like to acknowledge Hiroaki Ishihara for assisting us in the phantom experiment.

REFERENCES

[1] L. V. Wang and S. Hu, "Photoacoustic Tomography: In Vivo Imaging from Organelles to Organs," *Science*, **335**, pp. 1458-1462, 2012.

[2] M. Xu and L. V. Wang, "Photoacoustic imaging in biomedicine," *Rev. Sci. Instrum.*, **77**, pp. 041101-1-22, 2006.

[3] B. E. Treeby, E. Z. Zhang and B. T. Cox, "Photoacoustic tomography in absorbing acoustic media using time reversal," *Inverse Probl.*, **.26**, pp. 115003-115023, 2010.

[4] B. Cox, J. G. Laufer, S. R. Arridge and P. C. Beard "Quantitave spectroscopic photoacoustic imaging: a review," *J. Biomed. Opt.*, **17**, pp. 061202-1-22, 2012.

[5] S. R. Arridge, "Optical tomography in medical imaging," *Inverse Probl.*, **15**, pp. R41-R93, 1999.

[6] J. Laufer, B. Cox, E. Zang and P. Beard, "Quantitative determination of chromophore concentrations from 2D photoacoustic images using a nonlinear model-based inversion scheme," *Appl. Opt.*, **49**, pp.1219-1233, 2010.

[7] Z. Yuan, Q. Wang and H. Jiang, "Reconstrcution of optical absorption coefficient map of heterogeneous media by photoacoustic tomography coupled with diffusion equation based regularized Newton method," *Opt. Express*, **15**, pp.18076-18081, 2007.

[8] S. Okawa, T. Hirasawa, T. Kushibiki and M. Ishihara, "Numerical evaluation of linearized image reconstruction based on finite element method for biomedical photoacousitc imaging," *Opt. Rev.*, **20**(5), pp. 442-451, 2013.

[9] S. Okawa, T. Hirasawa, T. Kushibiki and M. Ishihara, "Reconstruction of the optical properties of inhomogeneous medium from photoacoustic signal with l_p sparsity regularization," *Proc. SPIE*, **8581**, 858135, 2013.

[10] C. R. Vogel, Computational Methods for Inverse Problems, The Society of Industrical and Applied Mathematics, 2002.

[11] S. Okawa, Y. Hoshi and Y. Yamada, "Improvement of image quality of time-domain diffuse optical tomography with l_p sparsity regularization," *Biomed. Opt. Express*, **2**(12), pp. 3334-3348, 2011.

[12] H. J. van Staveren, C. J. M. Moes, J. van Marie, S. A. Prahl and M. J. C. van Gemert, "Light scattering in Intralipid-10% in the wavelength range of 400-1100 nm," *Appl. Opt.*, **30**(31), pp. 4507-4514, 1991.

Quantification of optical attenuation coefficient based on continuous wavelet transform of photoacoustic signals measured by a focused broadband acoustic sensor

T. Hirasawa*[a], S. Okawa [a], M. Fujita [b], T, Kushibiki [a], M. Ishihara [a]
[a] Department of Medical Engineering, National Defense Medical College, 3-2 Namiki, Tokorozawa, Saitama, Japan;
[b] Second Division, Aeromedical Laboratory, Japan Air Self-Defense Force, 1-2-10 Sakae, Tachikawa, Tokyo, Japan;

ABSTRACT

We proposed a method of quantifying the effective attenuation coefficients of optical absorbers which uses the continuous wavelet transform to calculate the time-resolved frequency spectra of photoacoustic (PA) signals. In order to apply the method to blood oxygenation monitoring of blood vessels, this study discusses how to reduce the effects of blood vessel diameters, which influences on the time resolved frequency spectra of PA signals. Numerical simulations which calculate the PA signals produced from blood vessel phantoms with various diameters were performed. The simulations revealed that the frequency of PA signal became independent from the vessel diameters by measuring the PA signal from small area. The frequencies of simulated PA signals were proportional to the effective attenuation coefficients with a correlation coefficient of 0.99, and a slope of 0.035 MHz/cm^{-1} under condition that the measurement area was 4.0 mm at a frequency of 1.5 MHz. Thus we used the focused acoustic sensor of which focusing the foregoing measurement area. It consisted of a P(VDF-TrFE) film, which was characterized by broad frequency band. As results of experiments using the focused acoustic sensor, the frequencies of PA signals produced from blood vessel phantoms were proportional to the effective attenuation coefficients with correlation coefficient of 0.96 although the frequencies were suffered from deviations of 0.135 MHz, which corresponded to the effective attenuation coefficient of 3.46 cm^{-1}. Since the large deviations were caused by experimental factors such as sensor alignment, it is required to improve robustness to the experimental factors.

Keywords: Effective attenuation coefficient, Optical absorption coefficient, Functional monitoring, Blood oxygen saturation, Blood gas monitoring, Frequency analysis

1. INTRODUCTION

Photoacoustic imaging (PAI) technique is based on the generation of photoacoustic (PA) pressure waves, which generate ultrasound waves when optical absorbers absorb excitation light – generally, pulsed laser beams that satisfy thermal and stress confinement requirements [1]. These PA pressure waves propagate through biological tissues and can be measured as PA signals by acoustic sensors. PAI technique offers the spatial mapping of optical absorbers by calculating the distance between the acoustic sensors and optical absorbers from time delays of PA signals detection from the laser excitation time.

Optical absorption provides the dominant contrast in PAI, because intensities of PA signals produced by optical absorbers are generally proportional to amount of optical energies absorbed by the optical absorbers. Optical absorption coefficients of optical absorbers strongly depend on optical wavelengths. Since the dependences called optical absorption spectra varies with kinds of optical absorbers, PA images obtained at multiple optical wavelengths enable to determine the kinds of optical absorbers. The spectroscopic techniques called spectroscopic photoacoustic (sPA) [2] and other similar techniques [3] have been used to detect lipids in arterial wall [4], identify melanomas [5], and image exogenous contrast agents [6-9]. The techniques also enable to quantify the blood oxygen saturation by resolving deoxy-hemoglobin and oxy-hemoglobin in blood. Measuring the blood oxygen saturation in this manner has the advantages of higher spatial resolution and non-invasiveness compared to conventional methods such as pulse oximetry or gas analysis. To calculate the blood oxygen saturation from PA signals, the optical absorption coefficient or the effective attenuation coefficient of the blood should be quantified at each excitation wavelength. To quantify the coefficients, it is necessary to take account

* Takeshi Hirasawa : E-mail : hirasawa@ndmc.ac.jp, Telephone : +81 4 2995 1596

Photons Plus Ultrasound: Imaging and Sensing 2014, edited by Alexander A. Oraevsky, Lihong V. Wang,
Proc. of SPIE Vol. 8943, 89435Z · © 2014 SPIE · CCC code: 1605-7422/14/$18 · doi: 10.1117/12.2041676

of the optical energy densities (fluences) on optical absorber surfaces which also affect PA signals. Owingto strong optical scattering in biological tissues, however, the fluences on optical absorber surfaces are usually unknown. Thus, considerable attentions have been paid to developing methods for quantifying the coefficients [10].

Intensities of PA signals that proportional to amounts of optical energies absorbed by optical absorbers are used to quantify the optical absorption coefficients of the optical absorbers. Amounts of optical energies absorbed by the optical absorbers can be calculated as products of the optical absorption coefficients and the fluences on the optical absorber surfaces. Thus, the relative values of the optical absorption coefficients can usually be obtained by accounting for the fluences on the optical absorber surfaces. Model based techniques are proposed to quantify the coefficients. The techniques solve an inverse problem of the PA wave equation combined with the radiative transfer equation [11]. However, the techniques typically involve a computationally intensive iterative algorithm, making it difficult to quantify the optical absorption coefficients in real time.

To overcome these barriers, PA signal waveforms that depend on depth profiles of absorbed optical energies are used to quantify effective attenuation coefficients of optical absorbers [12-14]. Because optical energy attenuates exponentially along the light transfer axis in an optical absorber, PA signal waveforms detected along the light transport axis will have exponentially attenuated forms. Thus, the coefficients can be quantified by fitting the temporal waveforms to the exponential attenuation functions. One major advantage of the method is that the coefficients can be quantified on the basis of the relative temporal attenuation profiles of the PA signals, making it unnecessary to determine the fluences on the optical absorber surfaces. However, to quantify the accurate values of the coefficients, the PA signals should be measured by in two limited detection modes: near-field detection, in which the PA signals can be considered to be plane waves [13], and forward mode detection, in which the sample is irradiated by an excitation light source located on the far side of the acoustic sensor [12, 14]. Neither of these, however, is considered appropriate for measuring deep regions of thick biological tissue.

PA signal frequency spectra have also been used to derive the effective attenuation coefficients of optical absorbers [15]. The frequency spectra efficiently extract features of the PA signal waveforms. Because PA signals are unsteady pulsed waves, they have time varying frequency content; however, as the Fourier transform has no time resolution, only the time averaged frequency spectra are calculated. This blurs the temporal change of the frequency contents of the PA signals. Thus, we proposed the method to quantify effective attenuation coefficients which uses continuous wavelet transform (CWT) to calculate time-resolved frequency spectra from PA signal waveforms [16-18]. In the method, the maximum value of the dominant frequency calculated from time resolved frequency spectra was used to quantify the coefficient. We have already demonstrated that the frequency enable to quantify the coefficient using the planar optical absorber placed in transparent medium.

In this study, we discussed the application of the method to oxygen saturation monitoring of blood vessels. The application requires quantifying the effective attenuation coefficients independently from blood vessel diameters. However, the time resolved frequency spectra of PA signals were affected by geometries of optical absorbers. To reduce effects of blood vessel diameters onto PA signals, we proposed to detect PA signals from small area. Numerical simulations were performed using blood vessel phantoms with various diameters. Furthermore, we performed experiments using a focused acoustic sensor to detect PA signals from small area. To measure the broadband frequency contents of PA signals, the focused acoustic sensor made of P(VDF-TrFE) was used.

2. MATHERIAL AND METHOD

2.1 Continuous wavelet analysis of PA signals

The CWT is a spectral analysis method that can produce time-resolved frequency spectra of PA signals. The CWT modulus $T(a,b)$ is defined as the convolution of the temporal signal $p(t)$ and the dilated and temporally translated version of a wavelet function $\Psi(t)$ [19, 20]:

$$T(a,b)=a^{-\frac{1}{2}}\int_{-\infty}^{\infty}p(t)\Psi^{*}\left(\frac{t-b}{a}\right)dt, \qquad (1)$$

where $\Psi^{*}(t)$ is the complex conjugate of $\Psi(t)$, a is the dilation parameter, and b is the location parameter. Here, the complex Morlet wavelet, which is defined as a complex sinusoid with a Gaussian envelope, is used [19]:

$$\Psi(t) = \pi^{-\frac{1}{4}} \left(e^{-i\omega_0 t} - e^{-\omega_0^2 t} \right) e^{-\frac{t^2}{2}}, \qquad (2)$$

where ω_0 is central frequency of the wavelet, which determines number of sinusoidal waves within the Gaussian envelope. The dilation parameter a can be transformed into the frequency f using the equation $f = \omega_0/a$, where the time t replaces the location parameter b. Thus, the CWT produces time-resolved frequency spectra $T(f, t) = T(\omega_0/a, b)$ with a power given by $|T(f, t)|^2 = \mathrm{Re}[T(f, t)]^2 + \mathrm{Im}[T(f, t)]^2$.

The dominant frequencies of PA signals at each time points were calculated as the frequencies satisfying $d|T(f, t)|^2/df = 0$. The maximum value of the dominant frequency were calculated to quantify effective attenuation coefficients of optical absorbers [18].

2.2 Numerical simulation

To verify effects of vessel diameters onto maximum dominant frequencies of PA signals, PA signals produced from blood vessel phantoms with various diameters immersed in turbid medium were calculated by simulating both light transport and ultrasound propagation.

Figure 1(a) shows the geometry used in the numerical simulation. Blood vessel phantoms with wall thicknesses of 1 mm and inner diameters of 4.0, 5.0, and 6.0 mm were placed in a turbid medium. The tube phantoms were filled with six optical absorbers with different effective attenuation coefficients. The upper surface of the optical absorber was placed 8 mm away from the turbid medium surface. The optical properties of both turbid medium and optical absorbers were shown in Table 1. Both the reduced scattering coefficient and the optical absorption coefficient of the turbid medium correspond to that of typical biological tissues at NIR wavelength [21]. The coefficients of the optical absorbers corresponds to that of blood with an oxygen saturation of 0% to 100% at a wavelength of 756 nm [12, 22]. The acoustic sensor was contacted to the turbid media surface via 12 mm thick transparent medium.

The three-dimensional Monte Carlo light dosimetry software (3dgpu) developed by Lo and Lilge was used to simulate light transport in turbid medium [23]. The volume 15 x 15 x 25 mm within the turbid media was discretized into 300 x 300 x 500 voxels with sizes of 50 x 50 x 50 μm in x, y, and z directions. Propagation of 2 billion photon packets irradiated from top surface of the turbid medium were simulated to calculate the spatial distribution of absorbed optical energy $A(x, y, z)$.

PA signals produced from the blood vessel phantoms were calculated by solving PA wave equation. Assuming that the laser pulse widths are much shorter than the thermal diffusion time in the optical absorber and that acoustic inhomogeneity and viscosity of the medium are negligible, the PA wave equation can be given as [1]:

$$c^2 \nabla^2 p(\mathbf{r}, t) - \frac{\partial^2 p(\mathbf{r}, t)}{\partial t^2} = \frac{\beta c^2}{C_p} \frac{\partial H(\mathbf{r}, t)}{\partial t}, \qquad (1)$$

where c is speed of sound in the medium, β is the isobaric volume expansion coefficient, C_p is the specific heat, $p(\mathbf{r}, t)$ is PA pressure wave, and $H(\mathbf{r}, t)$ is the heat energy generated by optical absorption. The heat energy $H(\mathbf{r}, t)$ can be expressed as the product of the spatial distribution of the absorbed optical energy $A(\mathbf{r})$ and the temporal waveform of the laser pulse $\eta(t)$. The solution to Eq. 1 in the time domain can generally be expressed as [14, 18]:

$$p(\mathbf{r}', t) = \frac{\beta}{4\pi C_p} \left(\frac{1}{t} \iint_{|\mathbf{r}-\mathbf{r}'|=ct} A(\mathbf{r}-\mathbf{r}')\, dS \right) * \eta'(t) \qquad (2)$$

where $\mathbf{r}'$ is an observation point. The spatial distribution of absorbed optical energies $A(x, y, z)$ calculated by the light transport simulation was substituted into the Eq. 2. PA signals detected by a coaxial focused acoustic sensor with outer diameter of 6.0mm, inner diameter of 2.3 mm, and focal length of 25 mm were calculated. The dimension of the sensor was taken into accounted by performing a surface integration process in which the sensor was discretized into 3600 elements and then the PA signals detected by each element were calculated using Eq. 2. Finally, the individual signals were numerically integrated in order to calculate the total PA signal detected by the sensor surface. The measurement area of the sensor was 4.0 mm at a frequency of 1.5 MHz.

Time resolution of the entire simulation was limited by both voxel size of the light transport simulation and the time increment of the ultrasound propagation simulation. The voxel size of light transport simulation limits the time resolution

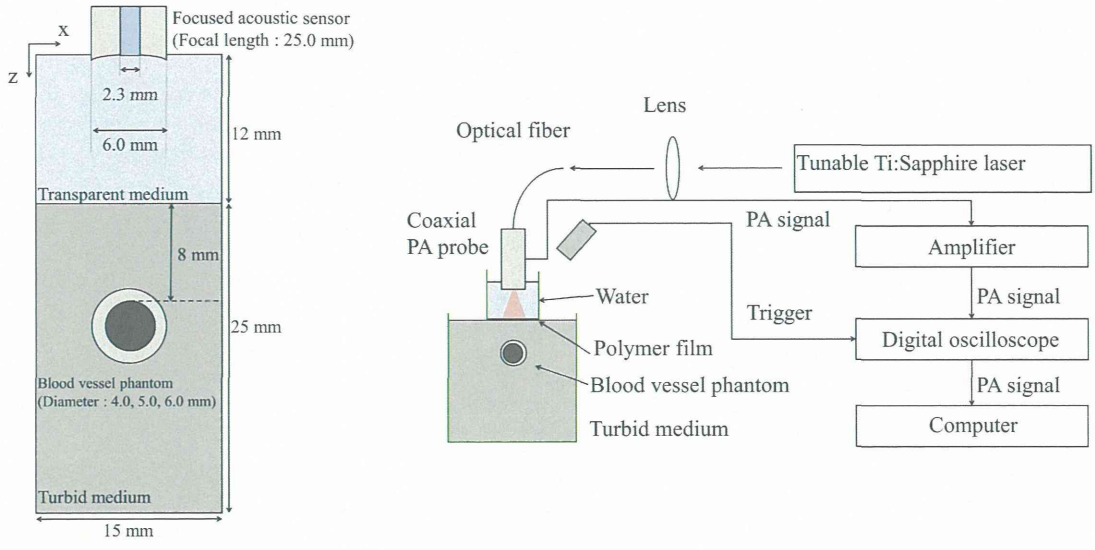

(a) (b)

Fig.1 (a) Geometry used in numerical simulation, (b) Schematic diagram of experimental setup

Table 1 Optical properties of optical absorbers and a turbid medium used in both experiment and numerical simulation

Location	μ_a (cm^{-1})	μ_s' (cm^{-1})	μ_{eff} (cm^{-1})	μ_s (cm^{-1})	g
Absorber 1	8.36	25.5	29.1	75.4	0.662
Absorber 2	7.29	25.5	26.8	75.4	0.662
Absorber 3	6.22	25.5	24.3	75.4	0.662
Absorber 4	5.15	25.5	21.8	75.4	0.662
Absorber 5	4.08	25.5	19.0	75.4	0.662
Absorber 6	3.01	25.5	16.0	75.4	0.662
Turbid medium	0.10	10.0	1.74	29.6	0.662

by the ultrasound propagation time within a voxel. The propagation time 57.7 ns was calculated by dividing the diagonal length of the voxels 86.6 μm by the sound speed 1500 m/s. Since the time increment of ultrasound propagation simulation 10 ns was smaller than 57.7 ns, the time resolution of the entire simulation was 57.7 ns. Therefore, the Nyquist frequency of the entire simulation was 8.66 MHz.

2.3 Experiment using phantoms

To experimentally verify the effect of vessel diameters onto the dominant frequencies of PA signals, we measured PA signals produced from blood vessel phantoms with various diameters and effective attenuation coefficients.

A reflection mode PA measurement system was used to measure PA signals produced from blood vessel phantom. In the reflection mode system, the excitation light irradiation and PA signal detection occur on the same side of the sample [18]. The schematic diagram of the experimental system is shown in Fig. 1(b). A tunable Ti:sapphire laser (LT-2211, Lotis Tii, Minsk, Belarus) pumped by the second harmonic of a Q-switched Nd:YAG laser (LS-2134, Lotis Tii, Minsk, Belarus) was used to produce excitation light pulses with a width of 10 ns and a repetition frequency of 15 Hz at a wavelength of 756 nm. The excitation light pulses were then coupled into a multi-mode optical fiber with a core diameter of 0.6 mm (M41L02, Thorlabs, Newton, NJ). The optical fiber was arranged coaxially relative to a specially designed ring-shape focused acoustic sensor. The focused acoustic sensor has ring-shape concave detection surface with focal